Mon. Not. R. Astron. Soc. **000**, 000–000 (0000) Printed 2 December 2011 (MN LATEX style file v2.2)

# Deep *Chandra* and *XMM-Newton* X-ray observations of AWM 7 – I: Investigating X-ray surface brightness fluctuations

J. S. Sanders and A. C. Fabian
*Institute of Astronomy, Madingley Road, Cambridge. CB3 0HA*

2 December 2011

**ABSTRACT**
We investigate the levels of small scale structure in surface brightness images of the core of the X-ray bright cool-core galaxy cluster AWM 7. After subtraction of a model of the smooth cluster emission, we find a number of approximately radial surface brightness depressions which are not present in simulated images and are seen in both the *Chandra* and *XMM-Newton* data. The depressions are most strongly seen in the south of the cluster and have a magnitude of around 4 per cent in surface brightness. We see these features in both an energy band sensitive to the density (0.6 to 5 keV) and a band more sensitive to the pressure (3.5 to 7.5 keV). Histograms of surface brightness in the data, when compared to realisations of a smooth model, reveal stronger surface brightness variations. We use the $\Delta$-variance technique to characterise the magnitude of the fluctuations as a function of length scale. We find that the spectrum in the 0.6 to 5 keV band is flatter than expected for Kolmogorov index fluctuations. If characterised by a power spectrum, on large scales it would have an index around $-1.7$, rather than $-3.7$. The implied 3D density fluctuations have a standard deviation of around 4 per cent. The implied 3D pressure variations are at most 4 per cent. Most of the longer-scale power in the density spectrum is contributed by the southern half of the cluster, where the depressions are seen. The density variations implied by the spectrum of the northern sector have a standard deviation of about 2 per cent.

**Key words:** intergalactic medium — X-rays: galaxies: clusters

## 1 INTRODUCTION

The velocity structure and degree of turbulence in the intracluster medium (ICM) of galaxy clusters is a matter of much debate as there are few direct observational constraints on its dynamical properties. The nonthermal contributions to gas pressure, if significant, are important to include for the determination of galaxy cluster masses from X-ray data. The viscosity and turbulence of the ICM have a bearing on how energy can be dissipated within the ICM, which connects to how the AGN can feed energy back into its environment (e.g. Kunz et al. 2011).

Theoretical calculations predict that the fraction of pressure support in the ICM from gas motions, generated by cluster growth and mergers, ranges from 5 to 20 per cent in the centres, increasing at larger radii (e.g. Lau et al. 2009; Vazza et al. 2009, 2011). Relaxed clusters have significantly lower amounts of turbulence than those merging or have recently merged, with turbulent pressure fractions of less than 10 per cent. However, the amount of turbulence in simulations depends crucially on transport processes such as viscosity or magnetohydrodynamical effects. The active galactic nuclei (AGN) in the centres of clusters are also often seen to be affecting the surrounding ICM, injecting jets and bubbles into the cluster (e.g. McNamara & Nulsen 2007) and likely causing gas motions. These generated motions have been predicted to range from 500 to 1000 $\mathrm{km\,s^{-1}}$ (Brüggen et al. 2005; Heinz et al. 2010).

One direct method of measuring or limiting gas motions in galaxy clusters is to examine the width of X-ray emission lines using the X-ray reflection grating spectrometer (RGS) on *XMM-Newton*. We recently placed a limit on ICM random gas motions in the core of Abell 1835 of 274 $\mathrm{km\,s^{-1}}$, at the 90 per cent level (Sanders et al. 2010). The implied limit on the turbulent to thermal energy density is less than 13 per cent. For a sample of objects we were able to find at least 15 sources with less than 20 per cent of the thermal energy density in turbulence (Sanders et al. 2011). This technique is, however, limited to sources with compact X-ray emitting cores and we can only examine the innermost regions. Other techniques to obtain limits or measure the velocity structure in clusters or elliptical galaxies includes examining the degree of resonance scattering in high resolution X-ray spectra (Werner et al. 2009), which imply strong upper limits on the gas motions.

Each of the above probes for gas motions indicates rather small amounts of gas motion in the cluster cores. There is additional indirect evidence that gas motions in the ICM are not strong in relaxed objects. These include the smooth changes in velocity of the filaments in the core of the Perseus cluster (Hatch et al. 2006),

which are apparently tracing gas motion (Fabian et al. 2003b) and their linear morphology.

Comparisons of X-ray and optical gravitational profiles in elliptical galaxies indicate additional non-thermal pressure contributions, some of which may be due to gas motions. The non-thermal pressure is around 10 per cent of the thermal gas pressure in M 87 and NGC 1399 (Churazov et al. 2008) or 20 to 30 per cent in a sample (Churazov et al. 2010). In the Perseus cluster, Churazov et al. (2004) found evidence from the existence of resonance line emissions for gas motions at around half the sound speed.

Schuecker et al. (2004) noted that for isotropic turbulence, like the velocity distribution, the pressure energy spectrum should have a powerlaw dependence with wave number. For the pressure, $E_P(k) \propto k^{-7/3}$ (see for example, section 6.9 in Lesieur 2008), rather than the standard 5/3 Kolmogorov relation for velocity. In three-dimensions (3D) this corresponds to a pressure power spectrum with a spectral index of $-13/3$. Schuecker et al. (2004) examined the spectrum of the fluctuations in a pressure map of the Coma cluster. They found that the spectrum between length scales of 40 and 90 kpc was well described by a projected Kolmogorov type spectrum. Integrating the spectrum after deprojection implied a lower limit of 10 per cent of the total ICM pressure in turbulence.

Churazov et al. (2011) recently reexamined *Chandra* and *XMM-Newton* data of the Coma cluster, finding that density variations in this object are rather small. The amplitude of the density fluctuations varies from 7 to 10 per cent on 500 kpc scales down to 5 per cent on scales of around 30 kpc.

In the interstellar medium, the electron density power spectrum as measured with interstellar scintillation is close to the value for a Kolmogorov process ($-11/3$) over at least five orders of magnitude (e.g. Armstrong et al. 1995). The spectral slope when observing HI 21cm line emission can vary, however. The value for the Small Magellanic Cloud is $-3.04$ (Stanimirovic et al. 1999), but measurements of the interstellar medium of dwarf galaxies gives slopes from $-1.5$ to $-2.6$ (Dutta et al. 2009).

Simulations of density fluctuations using hydrodynamics (Kim & Ryu 2005) found a Kolmogorov slope for low Mach numbers, flattening as the Mach number increased. For 3D compressible magnetohydrodynamical simulations of turbulence Kowal et al. (2007) found that the energy spectrum of density fluctuations with subsonic turbulence is consistent with $-7/3$ for strong magnetic fields and the Kolmogorov index of $-5/3$ for weak magnetic fields. For supersonic turbulence the density spectrum flattens, like the hydrodynamic simulations.

In this paper we use deep X-ray observations of a nearby ($z = 0.0172$) galaxy cluster AWM 7 to look for fluctuations in surface brightness which can indicate the degree of gas motions or turbulence. AWM 7 is an X-ray bright ($F_{2-10\,\mathrm{keV}} \sim 9 \times 10^{-11}\,\mathrm{erg\,cm^{-2}\,s^{-1}}$; Edge et al. 1992) poor cluster of galaxies located close to the edge of the Perseus galaxy cluster. The X-ray surface brightness is elongated along the east-west direction in the same direction as the Perseus-Pisces chain of galaxies (Neumann & Böhringer 1995). This is claimed to be caused by the infall of material along that direction rather than tidal effects. There is evidence for a clump of galaxies to the east of the cluster (Beers et al. 1995). The central dominant galaxy and central X-ray peak is offset 30 kpc to the west of the centre of the larger scale emission and the galaxy is aligned close to perpendicularly to the X-ray emission (Neumann & Böhringer 1995). The redshift of the central galaxy agrees with the cluster redshift and the cluster has a velocity dispersion of $\sim 730\,\mathrm{km\,s^{-1}}$ (Koranyi & Geller 2000). No significant velocity substructure is found (Koranyi & Geller 2002).

| Observatory | Observation | Date | Exposure (ks) |
|---|---|---|---|
| *Chandra* | 11717 | 2009-11-01 | 39.6 |
| *Chandra* | 12016 | 2009-11-03 | 22.3 |
| *Chandra* | 12017 | 2009-11-05 | 45.1 |
| *Chandra* | 12018 | 2009-11-06 | 26.8 |
| *XMM-Newton* | 0135950301 | 2003-02-02 | 31.6 |
| *XMM-Newton* | 0605540101 | 2009-08-16 | 126 |

**Table 1.** X-ray observations examined in this paper. Shown are the observatory, observation identifier, date of observation and exposure time. The exposure time shown is the full exposure for *Chandra* as all the data were used. For *XMM* the exposure is the average cleaned MOS exposure time.

Sato et al. (2008) found no evidence for bulk motions greater than the sound speed $\sim 1000\,\mathrm{km\,s^{-1}}$, using the *Suzaku* observatory. They found that the ICM temperature declines from a peak of 3.85 keV to 3.35 keV at 500 kpc. The cluster has a steeply peaked surface brightness profile, from which would be inferred a cooling rate of 20–35 $\mathrm{M_\odot\ yr^{-1}}$ in the absence of heating (Peres et al. 1998; Neumann & Böhringer 1995), and a cool 2 keV core (Furusho et al. 2003). The central mean radiative cooling time is short at 0.4 Gyr (Cavagnolo et al. 2009).

In this paper we restrict ourselves to an analysis of the surface brightness of the galaxy cluster AWM 7, leaving a spectral analysis to a future work. We assume, unless stated otherwise, that $H_0 = 70\,\mathrm{km\,s^{-1}\ Mpc^{-1}}$. At a redshift of 0.0172, 1 arcsec on the sky corresponds to 0.351 kpc.

## 2 OBSERVATIONS

### 2.1 Processing datasets

The galaxy cluster AWM 7 has been observed by both *Chandra* and *XMM-Newton*. Table 1 shows the observations we analyse in this paper. The *Chandra* observations were taken using the ACIS-I detector. All of the *Chandra* observations use the same aim-point. The *XMM-Newton* observations included the EPIC-MOS and PN detectors and the RGS instruments. We will mostly examine the *Chandra* data of the object in this paper, but also include the *XMM* EPIC-MOS data for confirmation. Although the EPIC-PN data could be used, the detector has numerous large chip gaps and a higher background than the MOS detectors, which make it more difficult to interpret.

We processed each set of data using standard software packages. The *Chandra* data were processed using the CIAO tool ACIS_PROCESS_EVENTS, using very faint mode grade rejection to reduce the background. The entire field of view of the ACIS-I detector was filled by the cluster and no additional front-illuminated CCDs were enabled. We therefore extracted lightcurves to check for flares from the edge of the ACIS-I array, as far as possible from the core of the cluster. We examined lightcurves in different energy filters (0.5–12, 0.5–2 and 2–12 keV) by eye, finding no evidence for any flaring. The different observations had consistent count rates. We therefore did not filter the *Chandra* datasets for flaring. Each event file was reprojected so that the physical coordinates matched the 12017 observation.

The *XMM-Newton* data were processed with SAS pipeline EMCHAIN. We filtered flares in the data using the lightcurve in the 10 to 15 keV band for events with a pattern of zero. Periods above 0.35 count per second were excluded for the MOS detectors. The coordinate system for dataset 0135950301 was reprojected to match the

| Observatory | Observations |
|---|---|
| *Chandra* | acis0iD2005-09-01bkgrnd_ctiN0001.fits |
| | acis1iD2005-09-01bkgrnd_ctiN0001A.fits |
| | acis2iD2005-09-01bkgrnd_ctiN0001.fits |
| | acis3iD2005-09-01bkgrnd_ctiN0001.fits |
| *XMM-Newton* | 1468_0504102401 MOS1 (-4), MOS2 (-5) |
| | 1500_0511011001 MOS1, MOS2 (-5) |
| | 1512_0505480701 MOS1 (-4), MOS2 (-5) |
| | 1548_0556200201 MOS1, MOS2 |
| | 1569_0553912001 MOS1 (-4), MOS2 |
| | 1587_0556214601 MOS1, MOS2 |
| | 1595_0551270201 MOS1 |
| | 1607_0510780201 MOS1 (-5), MOS2 (-5) |
| | 1796_0510780401 MOS1 (-5), MOS2 (-5) |
| | 1844_0604890201 MOS1 (-4), MOS2 |
| | 1935_0653870701 MOS1 (-4), MOS2 (-5) |
| | 2027_0412580701 MOS1, MOS2 |

**Table 2.** Background datasets used in this analysis. The *Chandra* data are standard blank-sky backgrounds identified using ACIS_BKGRND_LOOKUP. The *XMM-Newton* observations are closed-shutter particle background observations taken from `http://xmm.vilspa.esa.es/external/xmm_sw_cal/background/filter_closed/`. Shown are which MOS detector datasets were taken from each observation. In brackets are listed the excluded anomalous-state CCDs.

observation 0605540101. We used events with pattern values of 12 or less for the MOS detectors.

Point sources in the data were excluded from the data by eye. We examined the 0.5–2, 2–7 and 0.5–7 keV bands for point sources. We applied smoothing to identify fainter point sources, using smoothing scales of 6 and 8 arcsec. The excluded sources are shown as grey circles in Figure 1.

### 2.2 Background data

In order to get a good measurement of the surface brightness background subtraction can be important. For the *Chandra* data we used blank-sky background files (listed in Table 2). We combined the four background event files for the individual CCDs, reprojecting them to match the aspect of the observations. By adjusting the background exposure time, we normalised the count rate in the 10 to 12 keV band to match the observations.

The standard background files subtracted too much from the data however, leaving clear residuals. This was most apparent in the source-free 9 to 12 keV band. We found that the residuals were due to a mismatch between the bad pixels in the background and observation datasets. The bad pixel maps of the observations contained several more rows of bad pixels than were excluded from the standard backgrounds. To fix this, we created a list of the bad detector pixels which were common to the AWM 7 observations. We rejected any events in the background event files which had detector pixel coordinates in this list. After this filtering, in the high energy band there was a close match between the data and background files as expected.

The background subtraction of the *Chandra* data is not a critical part of the analysis, however. If no background subtraction is done, the features seen in surface brightness images do not change. In addition the spectra of fluctuation signal as a function of length scale (Section 4.4) do not change significantly. The use of blank sky backgrounds is not strictly correct, however, as AWM 7 lies in a region of low galactic latitude. The soft part of the background

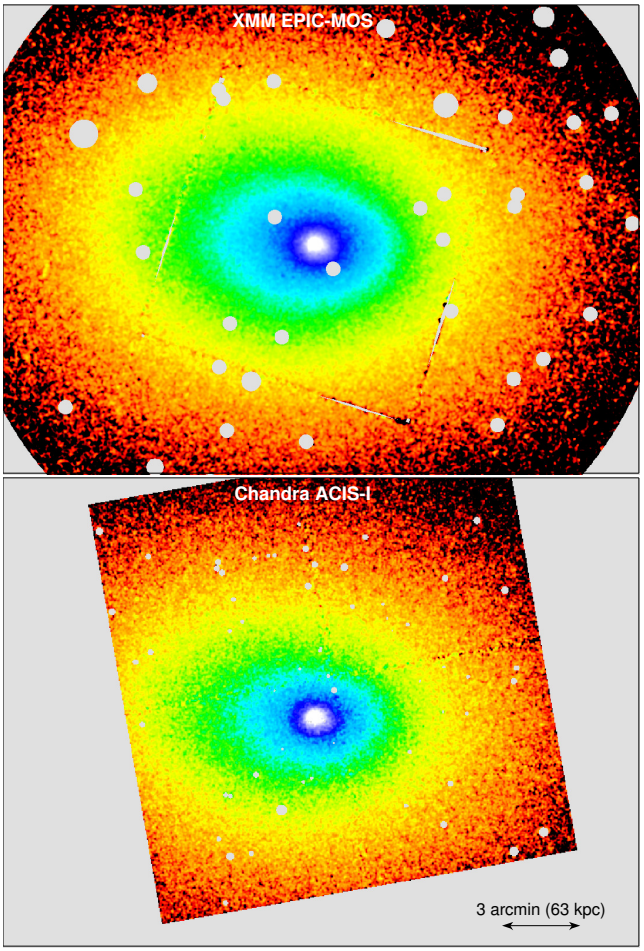


**Figure 1.** *XMM* EPIC-MOS and *Chandra* background-subtracted and exposure-corrected images of the cluster in the 0.6 to 5 keV band. The *XMM* data have a binning of 1.25 arcsec per pixel and the *Chandra* 1.968 arcsec. The data were smoothed by Gaussians of $\sigma = 2$ and 1 pixels, for *XMM* and *Chandra*, respectively. Excluded point sources and regions are shown in grey.

spectrum, particularly after the high energy count rate renormalisation, may be incorrect. Fortunately AWM 7 is a rather bright object. The 3.5 to 7.5 keV we examine later is the most sensitive to the background, but in this case it is dominated by particle background which we correctly subtract.

For the *XMM-Newton* data, which we examine only qualitatively, we subtracted the particle part of the background. We took recent closed-shutter EPIC-MOS observations (Table 2), excluding CCDs which were in the anomalous state (Kuntz & Snowden 2008). We filtered these data in the same way as the main observations and reprojected them to match the 0605540101 observation. A copy of this background was then reprojected to match the 0135950301 observation. We normalised the exposure of the background data in each CCD to match each observation count rate in the 9 to 12 keV band. We combined images of these background files in the same proportion as the 0135950301 and 0605540101 exposure times. We concentrate on the central MOS CCDs which are not affected by the anomalous state.

## 3 IMAGES

Fig. 1 shows the combined background-subtracted and exposure-corrected images of the cluster using the *XMM* EPIC-MOS (top panel) and *Chandra* data (bottom panel) in the 0.6 to 5 keV band. There are $6.9 \times 10^5$ events in this energy range in the central 3.5 arcmin radius in the *Chandra* data and $1.3 \times 10^6$ in *XMM* EPIC-MOS. For the *Chandra* data we exposure-correct using exposure maps weighted in energy using a 3.75 keV APEC $0.5\,Z_\odot$ spectral model (Smith et al. 2001), with an appropriate redshift and Galactic absorption. For *XMM-Newton* we produce exposure maps in the range of 0.8 to 1.6 keV around the Fe-L peak.

As can be seen in these images, the cluster has a smooth surface brightness profile. There is, however, structure within 1 arcmin radius of the central nucleus and there is a jump in the surface brightness profile around 3 arcmin to the west of the nucleus. This western edge can be seen in unsharp-masked images of the cluster in this band (Fig. 2 left panels; marked as Edge) and may be a poorly defined cold front.

To understand the effect of turbulence and gas motions, we would ideally want to study the 3D distribution of properties of the ICM, including the velocity, pressure, density, temperature and metallicity. Unfortunately these quantities are difficult to measure. The most accessible quantity is the X-ray surface brightness. The bolometric surface brightness closely probes the square of the density, integrated along the line of sight.

The energy band used is sensitive to different plasma properties, however. The 3.5 to 7.5 keV energy band can be used to examine variations in the integral of pressure-squared along the line of sight for temperatures between 1 and 3 keV (Forman et al. 2007). In Fig. 3 we show the temperature dependence of the surface brightness in this hard band and in a wider 0.6 to 5 keV band, at constant density and at constant pressure. For this simulation we used a Galactic column density of $10^{21}$ cm$^{-2}$ and the redshift of AWM 7. Typical temperatures in AWM 7 are $\sim 3.75$ keV, so the 3.5 to 7.5 keV energy band is not purely sensitive to the pressure-squared and has some temperature dependence. It is a better pressure-squared proxy than the 0.6 to 5 keV band. The 0.6 to 5 keV band has very little temperature dependence at constant density and is a good proxy for the integral of the density-squared along the line of sight.

We show in Fig. 2 (right panels) an unsharp-masked image in the 3.5 to 7.5 keV band, with the same smoothing parameters as for the 0.6 to 5 keV images in the left panels. The signal to noise ratio is lower in this image and we do not clearly see the edge that is apparent in the 0.6 to 5 keV unsharp-masked image. This may be because this band is more pressure sensitive and features are contact discontinuities, or that the signal to noise ratio is lower.

## 4 FLUCTUATIONS IN SURFACE BRIGHTNESS

We would like to remove the large scale cluster structure to examine the surface brightness variation on smaller scales. As the cluster is rather smooth and free of substructure, we model it by fitting ellipses to contours of surface brightness, spaced logarithmically. Model values for each pixel are calculated by linearly interpolating in logarithmic space the surface brightness between the two neighbouring ellipses. We mask out point sources and excluded sky regions in both the real and model images. We call the ellipse fitting and interpolation model ELFIT for the purposes of this paper. The ELFIT model removes both azimuthally symmetric emission and edge features, such as cold fronts, making it ideal to model the more subtle differences due to turbulent motions. In the 0.6 to 5 keV band we fit 20 ellipses and 10 in the 3.5 to 7.5 keV band.

| RA | Dec | Radius | Radius | Angle | $< r >$ |
|---|---|---|---|---|---|
| 43.614 | 41.579 | 13 | 17 | 103.3 | 3.7 |
| 43.613 | 41.577 | 35 | 47 | 81.2 | 10.9 |
| 43.614 | 41.578 | 70 | 95 | 81.2 | 22.6 |
| 43.622 | 41.578 | 121 | 181 | 91.8 | 43.4 |
| 43.633 | 41.578 | 186 | 274 | 84.8 | 71.2 |
| 43.635 | 41.579 | 267 | 376 | 82.1 | 99.3 |
| 43.628 | 41.578 | 356 | 484 | 81.8 | 129 |
| 43.629 | 41.575 | 447 | 612 | 86.5 | 162 |
| 43.577 | 41.431 | 951 | 1144 | 40.6 | 189 |

**Table 3.** Centres (J2000), radii (arcsec) and angles (deg) of the ellipses used for examining surface brightness distributions. We also show the mean radius in kpc from the cluster centre of the pixels between the ellipse and the ellipse interior to it (if any).

To construct a simulated image of the cluster, we take the smooth ELFIT model of the cluster, multiply by the exposure map of the real observation, add a background component and then make a Poisson realisation. This model dataset can be compared to the observed surface-brightness by background-subtracting and exposure-correcting. We can include fluctuations in the ELFIT model to see how detectable they are. Fig. 4 shows the real background-subtracted, exposure-corrected 0.6 to 5 keV and a simulated image of the cluster without any additional fluctuations. The ELFIT model does a good job at reproducing the overall surface brightness distribution. In our images we use a binning of four *Chandra* detector pixels (1.968 arcsec) per image pixel.

In Section 4.2 we will examine histograms of the surface brightness of the cluster as a function of radius. To do this we divide the cluster into regions using ellipses fitted to contours in surface brightness. The contours are placed logarithmically in surface brightness in the 0.5 to 7 keV band. They are shown in Fig. 4 and their properties are listed in Table 3.

### 4.1 Fluctuation images

Images of the model ELFIT surface brightness can be compared to the real surface brightness in detail. We smooth both the real data and the model with a Gaussian of $\sigma = 8$ pixels (15.7 arcsec), and then compute the fractional difference between the smoothed data and smoothed model. We also make a simulated dataset using the ELFIT model and compute the fractional difference between this simulation and the model. Fig. 5 shows the fractional differences in the 0.6 to 5 keV band of the real data (top-left panel) and simulated data to the model (bottom-left panel). There are features in the real data which are not visible in the simulated dataset. The most easily seen features are the apparent radial depressions from the south east of the image to the centre, and from the south-south-east to the centre.

The 3.5 to 7.5 keV band is sensitive to the pressure-squared. Fig. 5 (top-right panel) shows the fractional residuals between the real data and its ELFIT model, smoothing both by a Gaussian of the same size as was used for 0.6 to 5 keV. We also plot the fractional differences between a realisation of this model and itself in the lower-right panel. These data are much noisier than the 0.6 to 5 keV band, due to the lower number of counts and the higher level of background. Many of the features appear to match the wider

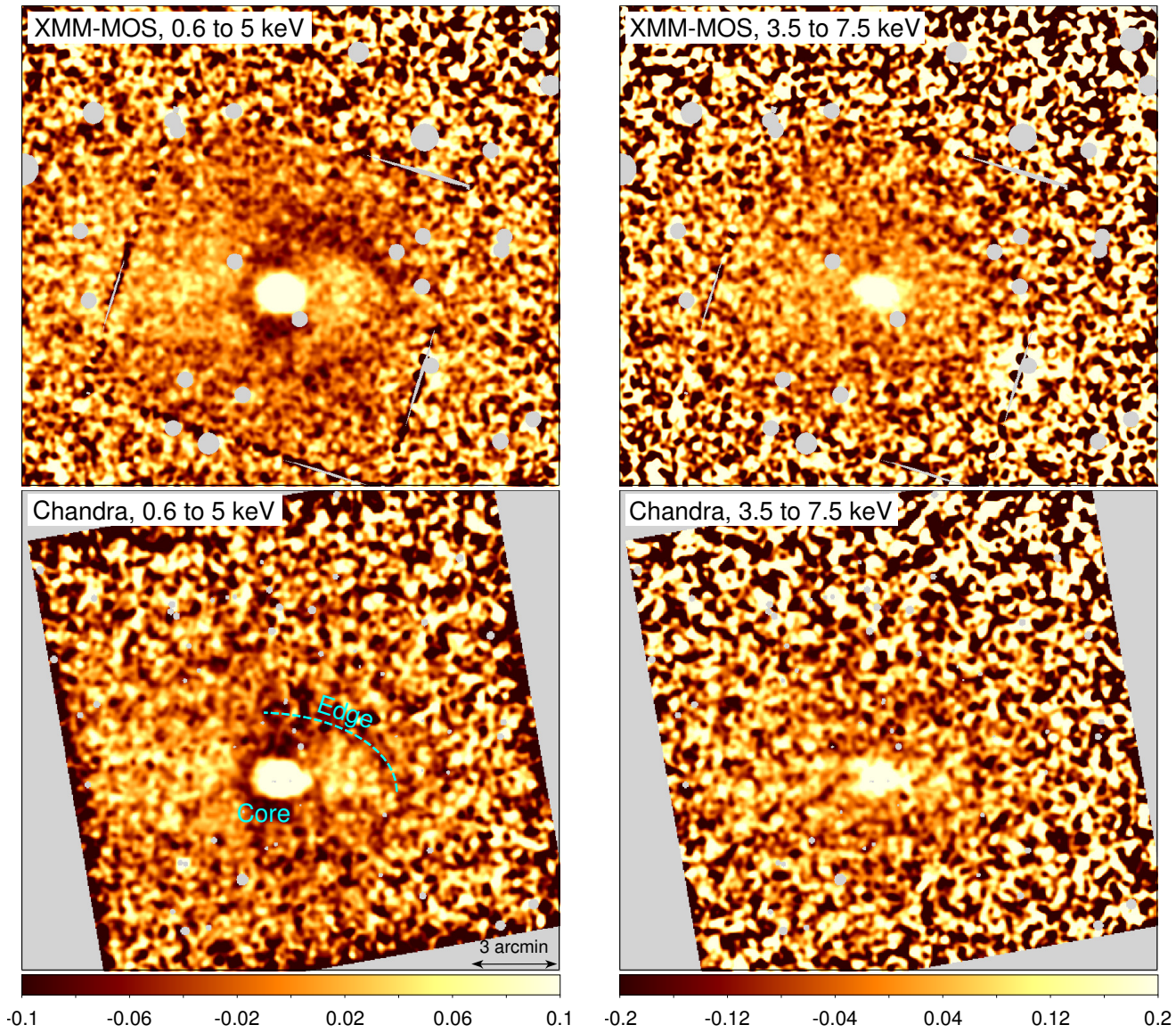


**Figure 2.** Unsharp-masked images of the cluster, in the density-sensitive 0.6–5 keV (left panels) and pressure-sensitive 3.5–7.5 keV bands (right panels). The top panels show the fractional difference between *XMM* EPIC-MOS data smoothed by Gaussians with $\sigma = 4$ and 32 1.25 arcsec pixels. The bottom panels show the results for *Chandra*, showing the fractional difference between images smoothed by Gaussians of 3 and 20 1.968 arcsec pixels. The bright central region is the central core which is saturated above the range shown.

band data, however, in particular the troughs in surface brightness in the south. The strength of the variations also appears to match the 0.6 to 5 keV band and is larger than the variations in the simulated data. It should be noted, however, that the two bands are not completely independent, although the wider band is dominated by softer emission.

We can also examine the *XMM-Newton* data to check that the deviations are not instrument-dependent. In Fig. 1 we showed the *XMM* EPIC-MOS combined background-subtracted, exposure-corrected image of the cluster. We similarly model the MOS image of the cluster with a 20 ellipse ELFIT model. Fig. 6 shows the fractional residuals of the data to the model surface brightness, after smoothing both by a Gaussian of 15 arcsec (12 pixels). It can be seen that the *Chandra* and *XMM* residuals match each other well, showing that many of the features are real deviations. The magnitude of the depressions to the south is around 4 per cent.

### 4.2 Pixel distribution histograms

A more quantitative measure of the structure in the surface brightness images can be made by examining the distribution of surface brightness as a function of radius. We investigate the distribution inside the ellipses listed in Table 3 (shown in Fig. 4). We smooth the data and ELFIT model with a Gaussian and compute a histogram of the fractional difference inside four neighbouring pairs of the ellipses. Point sources and regions outside that examined shown were filled with zero values before the smoothing. We investigated two

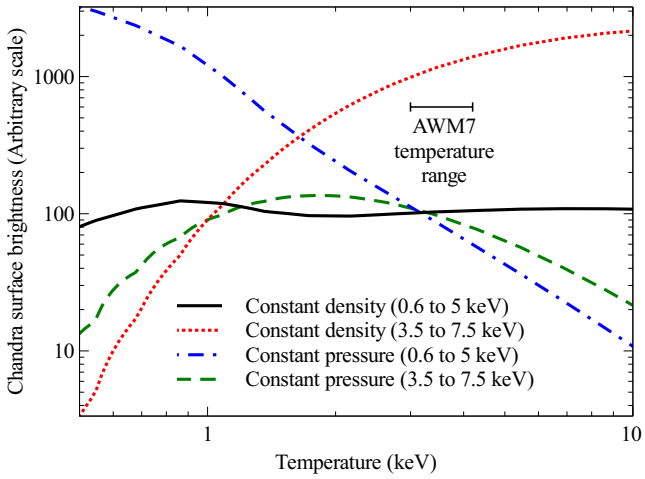


**Figure 3.** Variation in surface brightness as a function of temperature at constant density or pressure (similar to Figure 1 in Forman et al. 2007). The surface brightness in two bands, 0.6 to 5 keV and 3.5 to 7 keV are shown. The lines have arbitrary normalization. We also show the range of projected temperature in the region examined by our observations outside of the central core.

different Gaussian sizes, $\sigma = 2.8$ and 5.6 kpc, sensitive to fluctuations on these scales.

The fractional difference histograms relative to the ELFIT model are shown in Fig. 7. The rows show the results in ellipses increasing in radius and the columns show the effect of smoothing with two different Gaussian widths. The solid red line in each plot shows the surface brightness deviations of the real data relative to the ELFIT model. The dotted line and its blue surrounding shaded region shows the mean and standard deviation of 10 realisations of the ELFIT model to itself. The real data appear to have substantially wider distributions of pixel values than these model results. This difference is more apparent as more smoothing is applied.

The dashed line and green shaded region shows the mean and standard deviation of 10 realisations of the ELFIT model with Gaussian fluctuations added, relative to the ELFIT model. We generated the Gaussian fluctuations by convolving an image where the pixels were normally distributed, by a Gaussian of the size given, and scaling the size of the resulting fluctuations to have the correct standard deviation. The magnitude of these fluctuations is chosen to have a standard deviation of the model pixel values of 4 per cent. These distributions better reproduce the width of the data distributions, but the match is not exact. If the surface brightness fluctuations are of the order of 4 per cent, these correspond to 2 per cent fluctuations in projected density.

We show the distributions for the 3.5 to 7.5 keV band in Fig. 8. The differences between the smooth model and data are less apparent in this band, except when going to larger radii and applying more smoothing. In this plot we also display the results for a model with Gaussian fluctuations at the 8 per cent level, instead of 4 per cent.

The additional width of the distributions compared to the model confirm the fact that the maps appear to have additional fluctuations in the image above that expected from Poisson noise.

### 4.3 Cluster surface brightness modelling

The fluctuations presented above were revealed by the subtraction of an ELFIT cluster model. One potential problem with this approach is that we could be subtracting real signal from the data by including it in the model. The ELFIT model is good at removing features such as edges, which typically follow surface brightness contours. The method also removes shifts in the centres of isophotes as a function of radius or isophotal twists.

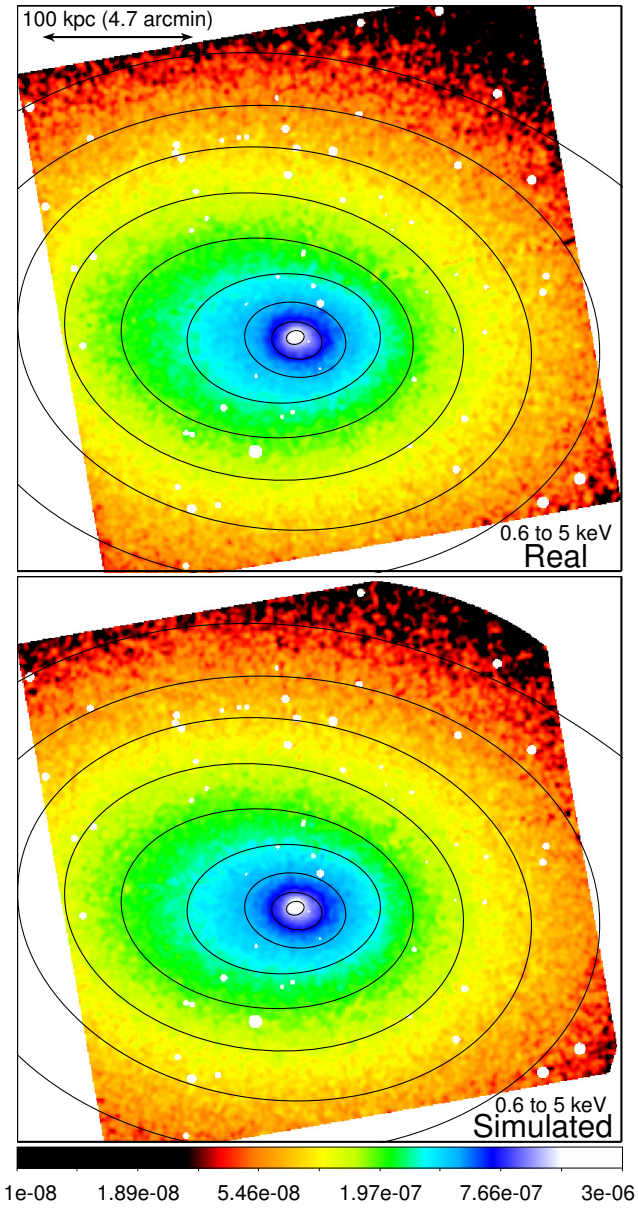


**Figure 4.** Real and simulated background-subtracted, exposure-corrected images of the cluster in the 0.6 to 5 keV band. The simulated data are a realisation of the ellipse fitting ELFIT model. The images have 1.968 arcsec binning and are smoothed by a Gaussian of $\sigma = 2$ pixels. The ellipses shown are fitted to the surface brightness and listed in Table 3.

In Fig. 9 is shown adaptively smoothed *Chandra* images of the cluster in the 0.6 to 5 keV band using the accumulative smoothing algorithm described in Sanders (2006). These images were produced using a variable-sized top-hat kernel with a radius chosen to include at least 225 counts at each position. Plotted in each image we display the jagged logarithmic-spaced surface brightness contours.

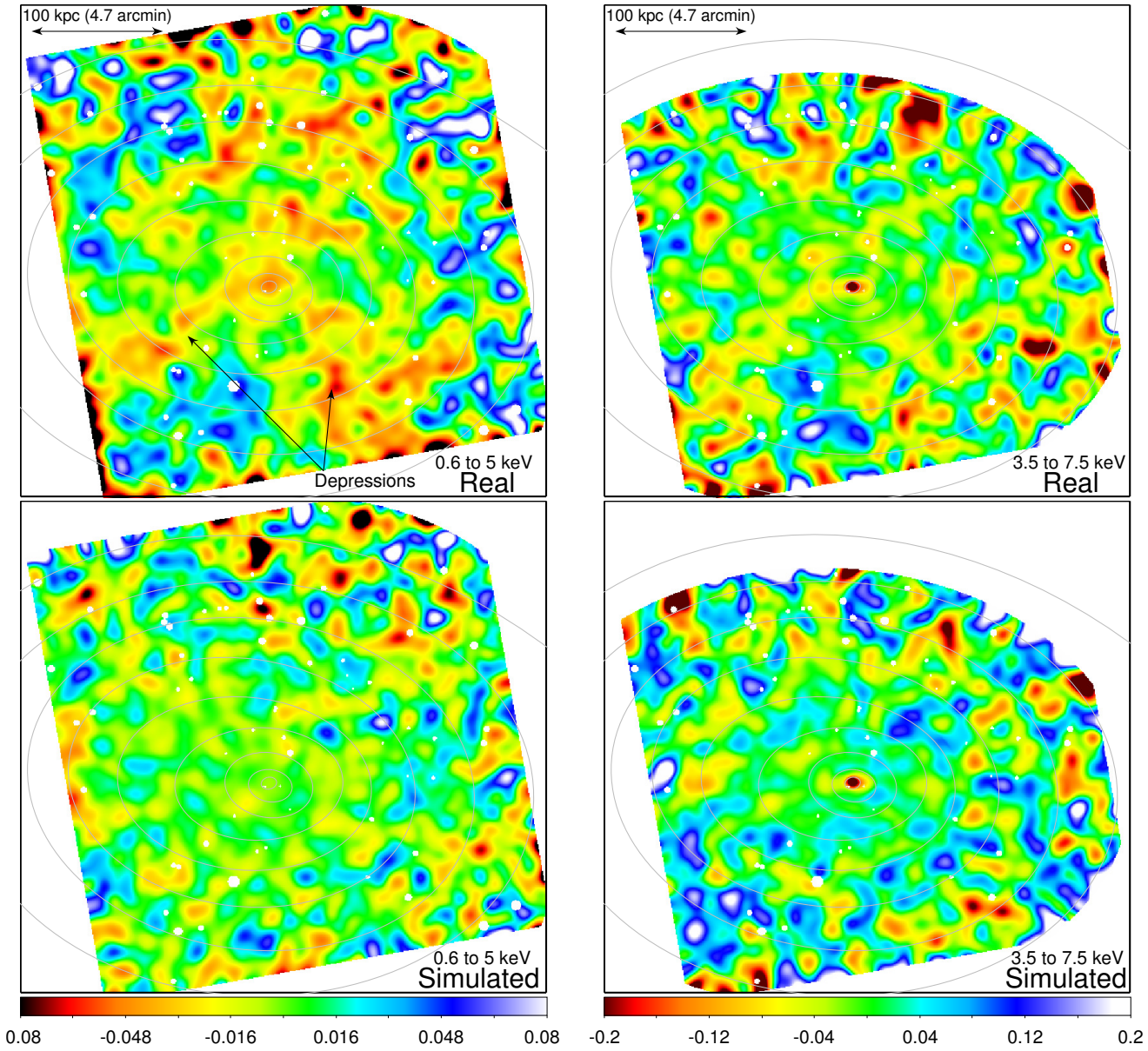


**Figure 5.** Fractional residuals between the *Chandra* data and the smooth ELFIT model, after smoothing both images with a Gaussian of $\sigma = 8$ pixels. The top panels show the results for the real data, whilst the bottom panels show the same analysis for a cluster simulated from the model. The left two panels show the residuals for the density-sensitive 0.6 to 5 keV band and the right two panels show the pressure-sensitive 3.5 to 7.5 keV range.

In the top panel of Fig. 9, we also show the contours of an elliptical $\beta$ model fitted to the surface brightness This model was fitted to the raw data using the CIAO SHERPA package, minimising the 'cstat' statistic, which takes account of the Poisson distribution of the counts. We excluded the central arcminute of the cluster from the fit (shown as a bold circle). The $\beta$ model was allowed to have a variable ellipticity, centre, core radius and index. The functional form of the surface brightness model used was

$$S(x,y) = S(r) = S_0(1+[r/r_0]^2)^{-\alpha} \quad (1)$$

for power law index $\alpha$ and core radius $r_0$, using

$$r(x,y) = [x_2^2(1-\varepsilon)^2 + y_2^2]^{1/2}/(1-\varepsilon), \quad (2)$$

where $\varepsilon$ is the ellipticity,

$$x_2 = (x-x_0)\cos\theta + (y-y_0)\sin\theta, \text{and} \quad (3)$$

$$y_2 = (y-y_0)\cos\theta - (x-x_0)\sin\theta, \quad (4)$$

where $\theta$ is the angle of ellipticity and $(x_0, y_0)$ are the coordinates of the centre.

The model is a reasonable fit to the surface brightness on larger scales (i.e. there is a close match between the contours of the data and model), but there are quite large offsets around the core of the cluster between the model and data, particularly to the west of the core and a depression beyond that. These residuals can be seen in the fractional difference between the adaptively smoothed data and the model (Fig. 10, top panel). As noted by Neumann &

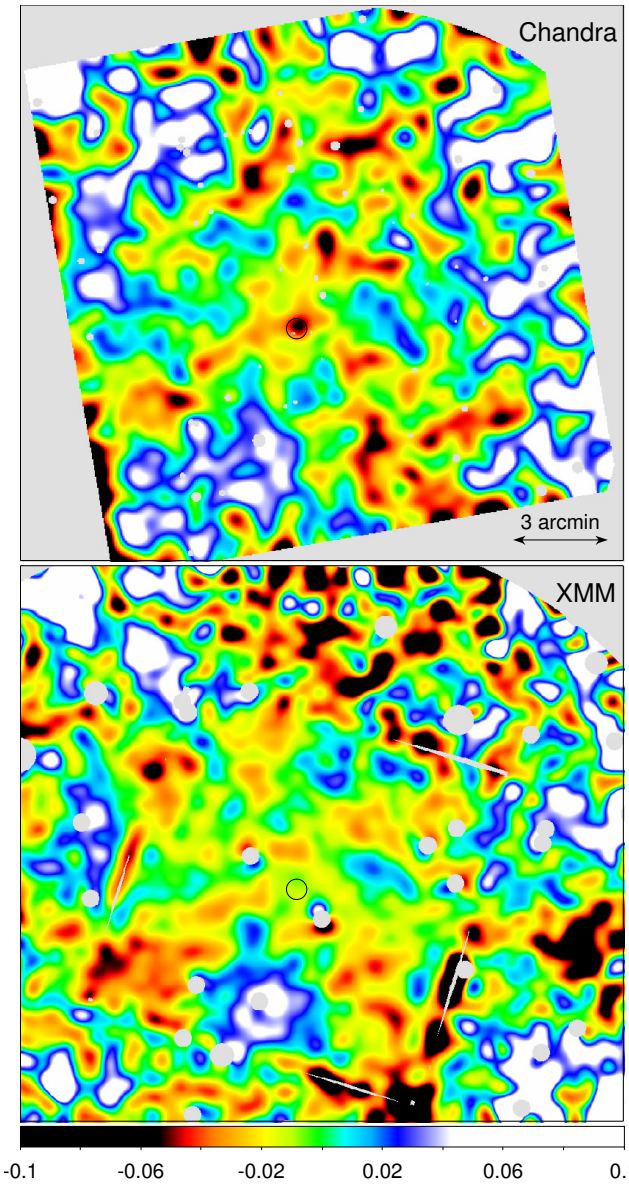


**Figure 6.** Fractional differences of the *Chandra* and *XMM* EPIC-MOS background-subtracted, exposure-corrected images to their respective ELFIT models in the 0.6 to 5 keV band. The data and models have been smoothed by 8 and 12 pixels, for *Chandra* and *XMM*, respectively. The black circle marks the X-ray peak of the cluster.

Böhringer (1995), the central X-ray peak is offset from the outer parts of the cluster.

In the second panel of Fig. 9, we show contours from a two-component $\beta$ model fit to the surface brightness. In this fit we did not exclude the central core. Each $\beta$ component was allowed to have free centre, core radius, index and ellipticity during the fitting. The two-component model is a better fit to the data than the single-component model, although there are discrepancies, particularly around 3 arcmin north of the core and 5 arcmin to the west. The residuals, shown in Fig. 10, are smaller than the single-component $\beta$ model, but have a similar morphology.

The bottom two panels of Fig. 9 show the comparison between

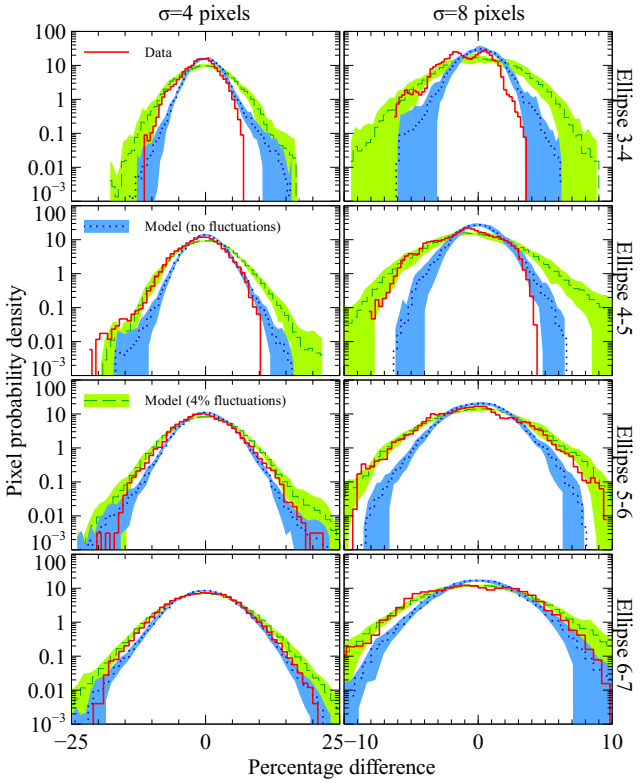


**Figure 7.** Distribution of surface brightness in the 0.6 to 5 keV band in different regions relative to the ELFIT model, after smoothing. The rows show the results between four pairs of ellipses, with increasing radius. The columns show the results after smoothing with Gaussians with $\sigma = 4$ and 8 pixels (2.8 and 5.5 kpc). In each panel, the thick solid red line shows the real data. The dotted line and its surrounding blue shaded region shows the mean and standard deviation for realisations of the smooth ELFIT model itself. The dashed line and its green shaded area shows the distribution for realisations of the ELFIT model plus Gaussian fluctuations of 4 pixel scale and a level of 4 per cent.

ELFIT models using 10 and 20 ellipses. These models are better fits than the $\beta$ models, as expected if the isophotes are approximately elliptical. The residuals on larger scales, shown in Fig. 10, are substantially reduced from the $\beta$ model fits. The 20 ellipse model is better at fitting the edge an arcmin to the east of the core than the 10 ellipse model.

The residuals in Fig. 10 for the $\beta$ model fits do not resemble the structures expected in the presence of simple hydrodynamic turbulence (see Section 5).

### 4.4 Spectra of fluctuations

It is useful to characterise the scale on which any fluctuations occur. The $\Delta$-variance method (Stutzki et al. 1998) measures the variance in a two-dimensional image on a specific length scale. The technique was recently used to examine X-ray observations of the Coma cluster (Churazov et al. 2011). In its simplest form it works by filtering an image with a wavelet Mexican or French hat function with a particular size and computing the variance of the pixels. Pixels outside of the region of interest can be easily excluded in the analysis by the use of a weighting map. The weighting map is also convolved by the same function to allow the effect of any edges to be removed.

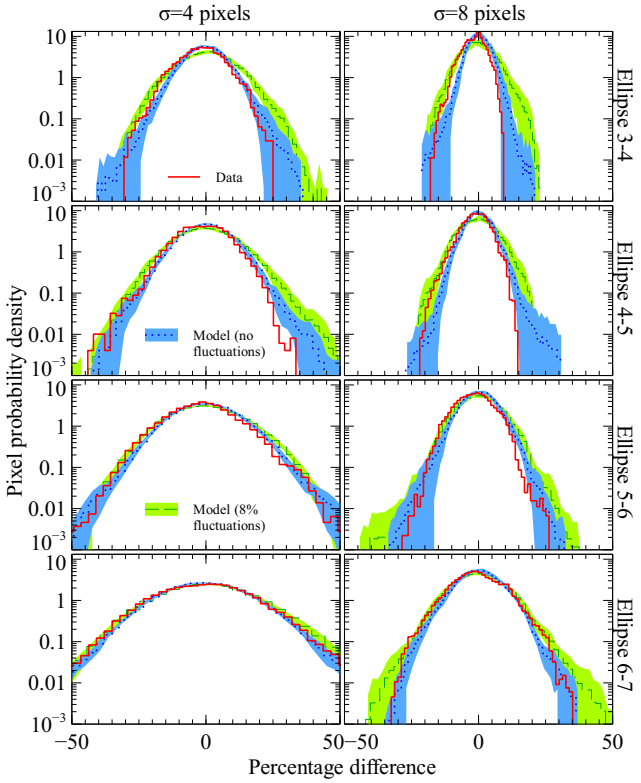


**Figure 8.** Distribution of surface brightness in the 3.5 to 7.5 keV band in different regions relative to the ELFIT model, plotted in the same way as Fig. 7. The dashed line and shaded regions in this plot show a model with Gaussian fluctuations of 4 pixel scale and a level of 8 per cent added.

We compare the Δ-variance spectra with spectra of cluster models, where we add different levels of fluctuations. We use two different types of fluctuation field. The first fluctuation type is simple Gaussian fluctuations on the projected surface brightness. These are characterised by a Gaussian length scale, $\sigma$, and the standard deviation of the fluctuation field, expressed as a percentage on the underlying cluster surface brightness (generated using the method described in Section 4.2).

The second type of fluctuation model we use is generated using a powerlaw power spectrum. To make the power spectrum fluctuation models, we used an inverse fast Fourier transform of a 3D cube where each pixel was scaled by the power spectrum, but with a normal distribution of the real and imaginary components. We used a cube size of 700 pixels along each axis, which was larger in each dimension than the *Chandra* image of the cluster. We took the real component of the pixels after the inverse transform, scaling them so that the standard deviation of the fluctuations was of the magnitude required (the values of such a field have a Gaussian distribution). Parseval's theorem says that the variance of the pixel distribution should be equal to area under the power spectrum. Fig. 11 (top panel) shows a slice through an example 3D field after normalising it to have a standard deviation of 1.

We examine models with power spectral indices of $-11/3$ and $-13/3$ in 3D. We compare the $-11/3$ models with the density-squared-sensitive 0.6 to 5 keV band and the $-13/3$ models with the pressure-squared-sensitive 3.5 to 7.5 keV band. We truncated the power spectrum to zero on scales of larger than 150 kpc.

To compute the projected model we project the 3D field using a deprojected cluster emissivity model of the galaxy cluster. We

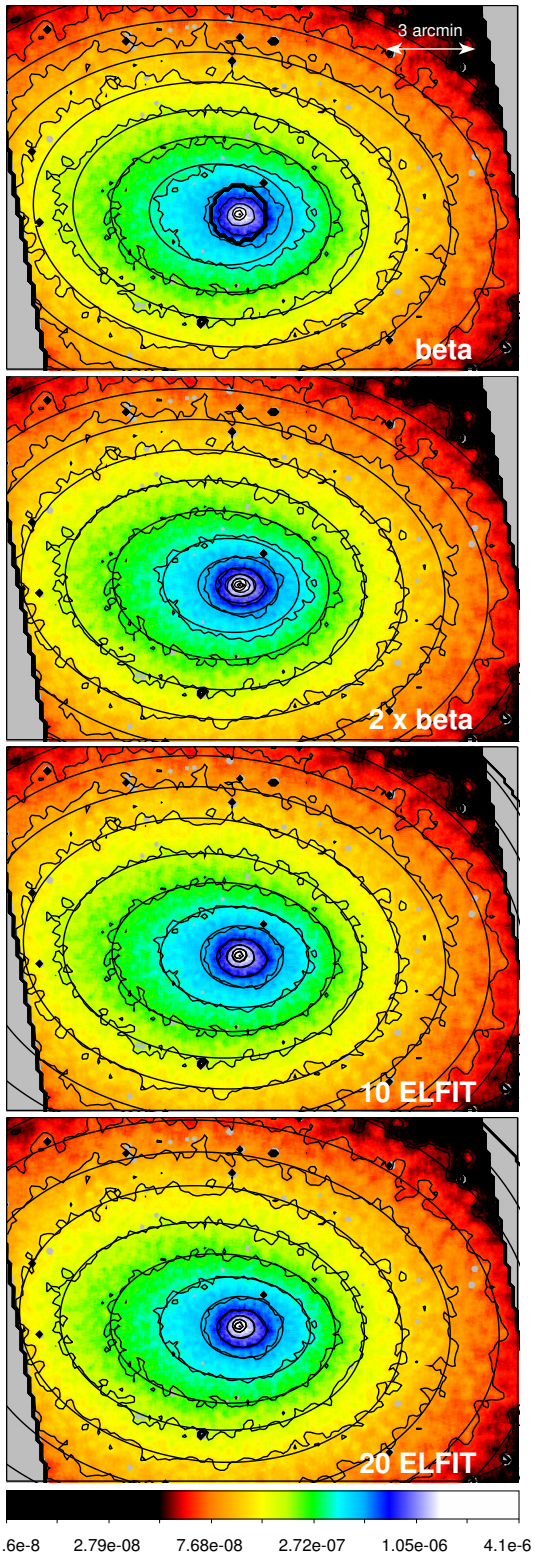


**Figure 9.** Adaptively-smoothed exposure-corrected *Chandra* image in the 0.6 to 5 keV band. Contours of surface brightness are plotted (20 logarithmic contours from $1.2 \times 10^{-8}$ to $3 \times 10^{-6}$, appearing ragged). The smooth contours are of a fit using a $\beta$ model excluding the core (first row), a double-$\beta$ model including the core (second row), and 10 and 20 ellipse ELFIT models (third and fourth rows, respectively).

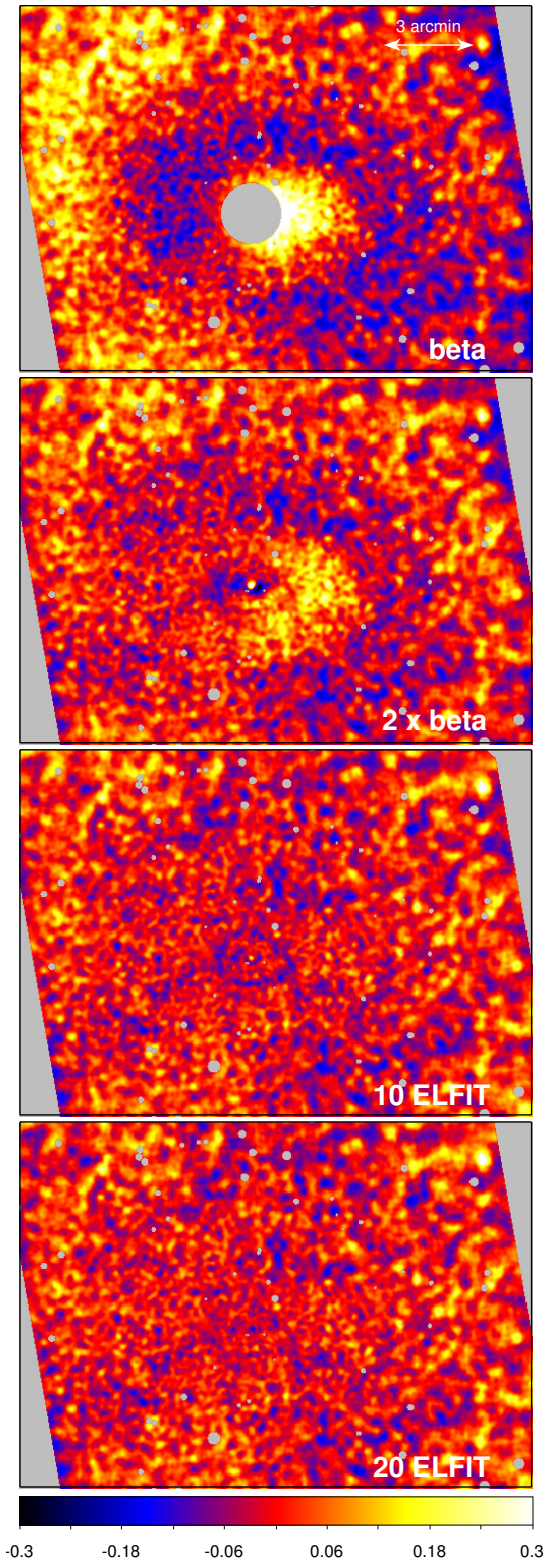


**Figure 10.** Fractional residuals between adaptively smoothed data and models, for the models shown in Fig. 9.

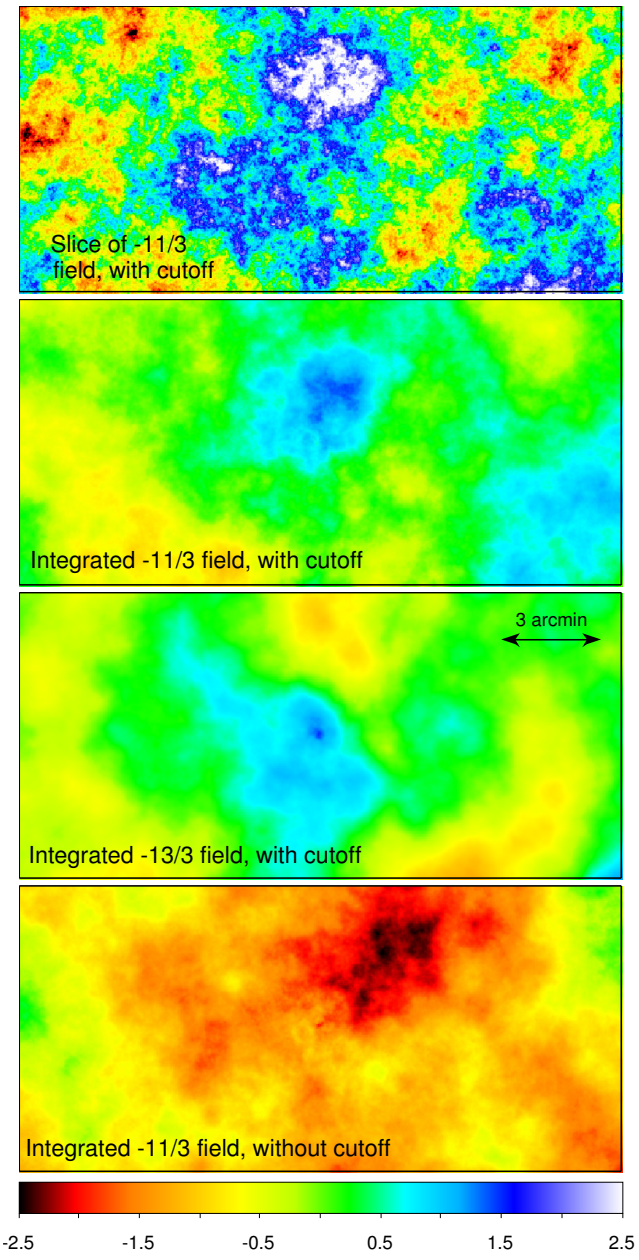


**Figure 11.** (Top panel) 2D slice through a 3D random field with a power spectral index of $-11/3$. We removed power on scales of larger than 150 kpc. This field has a standard deviation of 1 in 3D. (Centre top panel) The same field, after integrating along the line of sight, taking account of the cluster emissivity profile. (Centre bottom panel) A field with a power spectral index of $-13/3$ integrated along the line of sight. (Bottom panel) A field with a power spectral index of $-11/3$, with no large scale cut-off, integrated along the line of sight.

take the average 2D surface brightness profile of the cluster from the *Chandra* image in the 0.5 to 7 keV band and deproject it assuming spherical symmetry to compute the emissivity. We integrate the 3D fluctuation field along a line of sight when it is applied to the 3D emissivity model. Expressed mathematically, this is

$$S(x,y) = \int [1+\varepsilon F(x,y,z)] E(x,y,z)\,\mathrm{d}z, \quad (5)$$

where $S(x,y)$ is the surface brightness on the sky at position $x,y$, $E(x,y,z)$ is the cluster emissivity model, $F(x,y,z)$ is the fluctuation field normalised to have a standard deviation of 1 and $\varepsilon$ is the size of the fluctuations required, expressed as a percentage. The fluctuations produced by the projection are shown in Fig. 11 (centre top panel). For a particular value of $\varepsilon$, the area under the power spectrum is $\varepsilon^2$.

We also show an example field in the centre-bottom panel of Fig. 11 with a powerlaw power spectral index of $-13/3$, which is more appropriate for the pressure of turbulent material. This field includes the same large scale cut-off. In bottom panel we show the effect of removing the large scale cut-off. Large regions of the image are reduced or enhanced retaining these scales.

If the power spectrum follows a powerlaw,

$$P(|\mathbf{k}|) \propto |\mathbf{k}|^{-\xi}, \tag{6}$$

the $\Delta$-variance should also also give a powerlaw behaviour, where

$$\sigma_\Delta^2 \propto L^{\xi-2}, \tag{7}$$

for length scale $L$, if $0 \leq \xi < 6$ (Stutzki et al. 1998). Note that this is not realised in practice here because the ELFIT cluster model we later subtract from the data removes some larger scale power. We use the method with a Mexican hat filter with a ratio of the sizes of the core and annulus of 1.5 (Ossenkopf et al. 2008). With this kernel, the probed scale is a factor of 1.075 larger than the size of the kernel. We multiply the kernel size by this factor when plotting $\Delta$-variance spectra.

In the top-panel of Fig. 12 we show the $\Delta$-variance spectrum of the exposure-corrected 0.6 to 5 keV data in the 1 to 6.7 arcmin radial region. On this and our other $\Delta$-variance spectra the units are $(\mathrm{photon\,cm^{-2}\,s^{-1}})^2$. On short length scales the signal is dominated by the Poisson noise and on long scales by the overall morphology of the cluster. In Fig. 12 we also plot the spectra of simulated cluster images using the 20 ellipse ELFIT model, with different levels of fluctuations added. For each model we show the mean spectrum for 10 realisations of the model. The shaded regions around each line shows the standard deviation of the models. The region indicated 'smooth model' is the elliptical model realisation without additional structure. The Gaussian models add projected fluctuations with a standard deviation of 8 per cent to the smooth model, on scales of 2.8 and 5.5 kpc. The powerlaw models show the smooth model with $-11/3$ power spectral index fluctuations of the standard deviation shown in 3D. The models show increasing amounts of signal on long length scales, as the standard deviation is increased, as would be expected. The smooth model spectrum is slightly larger than the data on long length scales. This is more easily seen when subtracting the smooth model spectrum from the data and other models, seen in the second panel. Subtracting the smooth model removes most of the effect of the cluster shape and the Poisson noise.

In the third panel of Fig. 12 we show the effect of removing the 150 kpc cut-off in the model power spectra. With this cut-off removed, the fluctuations in the models are both positive and negative. This is because the large scale fluctuations on long length scales depress or enhance the surface brightness in the region examined. This negative fluctuation distribution can still be seen in the models with the cut-off in the second panel. The bottom panel shows the effect of modelling the cluster with a double-$\beta$ model fit instead of the ELFIT model. The data show more structure on large scales than this model (as seen in Fig. 10).

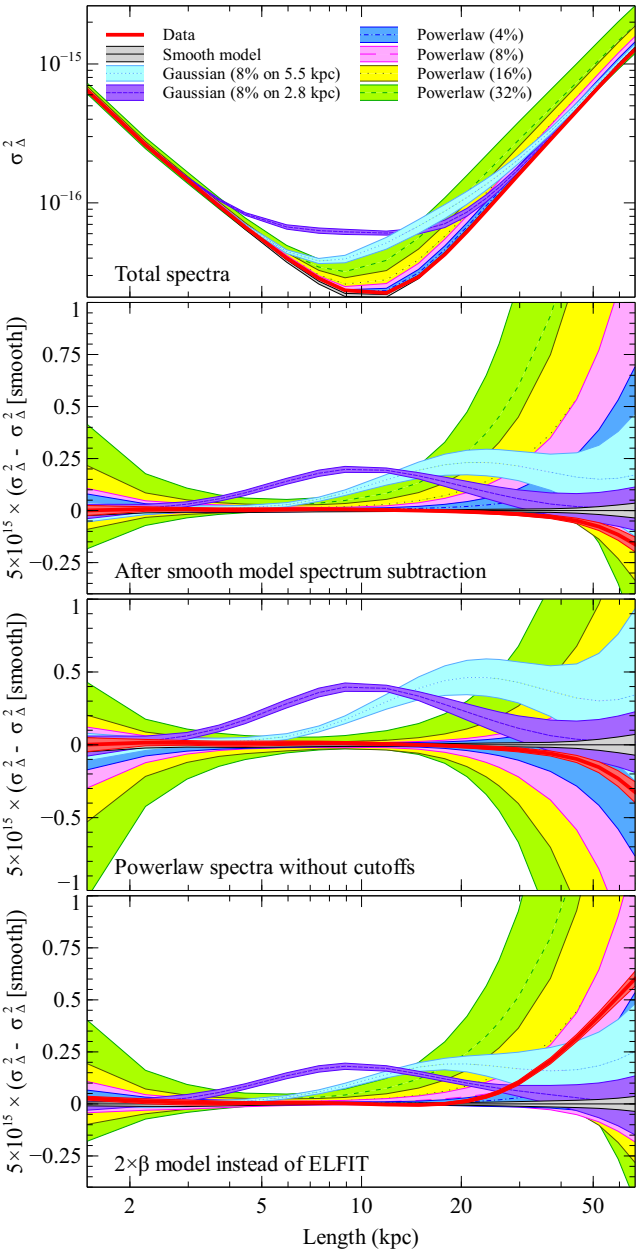


**Figure 12.** (Top panel) $\Delta$-variance spectra of the 0.6 to 5 keV cluster data and ELFIT-based model realisations, between 1 to 6.7 arcmin radius. The units of the $\Delta$-variance spectra are $(\mathrm{photon\,cm^{-2}\,s^{-1}})^2$. The different lines show models with either added Gaussian projected fluctuations, or noise with a powerlaw spectral index of $-11/3$. (Second panel) Spectra after subtracting the spectrum of the smooth model. (Third panel) Comparison with models where we do not cut off the power spectrum on long length scales. (Bottom panel) Results calculated using a $2 \times \beta$ model rather than the ellipse model for modelling the cluster surface brightness.

### 4.5 Spectra after subtraction of smooth cluster model

We can learn more by removing the dominant contribution on large scales, by subtracting a smooth cluster model before calculating the $\Delta$-variance spectra. Some care must be taken when doing this because the smooth model is based on a fit to the data. We should treat a smooth model with fluctuations added in the same way as the data when comparing their spectra. To do this, for each realisation of a

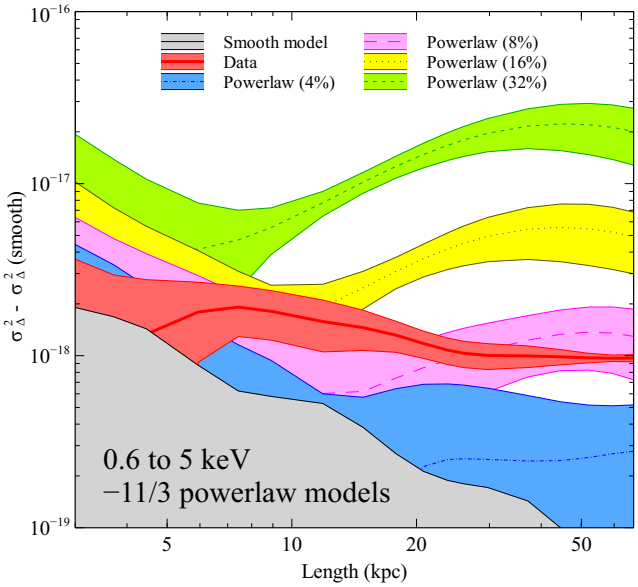


**Figure 13.** Δ-variance spectra of the data and simulated images with increasing levels of powerlaw spectral fluctuations added. The plot shows the 0.6 to 5 keV band and 1 to 6.7 arcmin radial regions. The smooth ELFIT model was subtracted from the images before computation of the spectra. Poisson noise in the spectra was removed by subtracting the mean spectrum of ELFIT model realisations. The grey shaded region shows the standard deviation of the subtracted model. The red line shows the spectrum of the data. The blue, pink, yellow and green curves show, respectively, the spectra of model clusters with 4, 8, 16 and 32 per cent, $-11/3$ index power spectra emissivity fluctuations added.

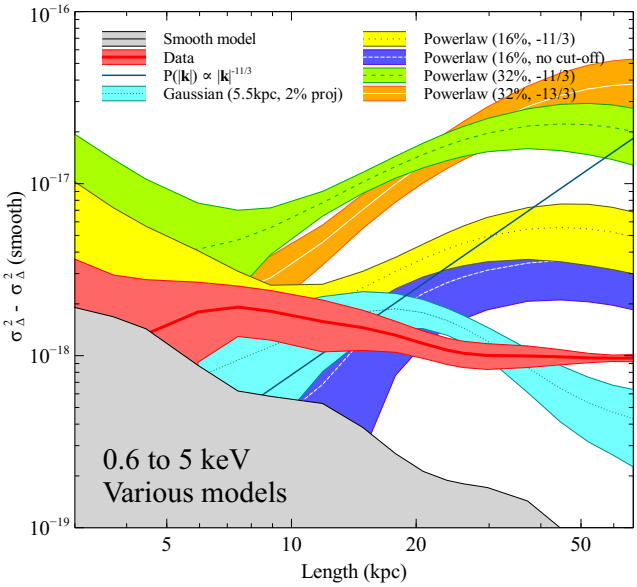


**Figure 14.** Data spectrum from Fig. 13, plotting additional models. The expected spectrum of $-11/3$ fluctuations is shown as a solid line. Note that the expected spectrum is not achieved for the model spectra because the subtraction of the fitted model of the cluster cuts off the spectra on long scales. Also shown in cyan is the spectrum of an ELFIT model with Gaussian fluctuations at the 2 per cent level on scales of 5.5 kpc. The spectra of $-11/3$ powerlaw power spectral models with and without the cut-off on large scales, with 16 per cent fluctuations, are shown in yellow and purple, respectively. The spectra of 32 per cent fluctuation models with $-11/3$ and $-13/3$ spectral indicies, are plotted in green and orange, respectively.

model with fluctuations added, we refit the realised model in the same way as the data, before subtraction of that fitted model. With this method, if the fitted model subtracts away real signal from the data, we will also do it for the simulated model, making comparison of the spectra valid.

We show the Δ-variance spectra of the data and simulated clusters with added powerlaw power spectrum fluctuations in Fig. 13, examining the 0.6 to 5 keV band image between 1 and 6.7 arcmin radius. After the ELFIT subtraction, it is much easier to differentiate the different models. In this graph we plot the spectra logarithmically, as the error bounds of the signals are positive. The shaded grey region at the bottom of the plot shows the standard deviation of the spectra of 10 different ELFIT model realisations. This region is the minimum uncertainty on the spectra and shows the region below which signals become statistically insignificant. The red line is the spectrum of the data and the shaded red region is the standard deviation on the smooth model realisation results, used as an estimate of the data spectrum uncertainty.

On this plot we include the spectra for realisations of ELFIT models with added powerlaw power spectral fluctuations using a standard Kolmogorov index of $-11/3$. We show the model spectra with normalisations of 4, 8, 16 and 32 per cent (shown in blue, pink, yellow and green, respectively). The normalisations were defined previously to be the standard deviation on the emissivity fluctuation distribution.

It can be see that the fluctuations in the data are detected on scales above 5 kpc. The data spectrum does not closely match any of the model spectra, but is most similar to the model with 8 per cent fluctuations (shown in pink). The shape of the data spectrum is also rather flat or even negative. If the data were characterised by a power spectral slope, it would be much flatter at around $-1.9$, plotting Equation 7, rather than $-11/3 \sim -3.7$.

In Fig. 14 we show the data spectrum with different spectral models to show the effect of various factors. We show 32 per cent fluctuation models with power spectral indices of $-11/3$ (green) and $-13/3$ (orange). Over the central ranges of length scale these models can be clearly distinguished. The solid line in the plot shows the expected spectrum for $-11/3$ fluctuations using Equation 7. We do not get the same slope as this line on large length scales because the ELFIT models removes some of the fluctuations on these scales. We also plot a 16 per cent fluctuation model, but show the effect of including (yellow) and removing (purple) the cut-off on larger scales in the power spectrum. Without the cut-off the distribution the distribution of the spectra for the models becomes wider, as discussed in Section 4.4. By removing the signal above 150 kpc, we boost the signal below these length scales when normalised to the same standard deviation. Finally, we show the non-physical Gaussian fluctuation model (cyan). It gives a similar signal to the data, but has less power on long length scales.

If we examine the 3.5 to 7.5 keV data for the same spatial region, we obtain the spectra in Fig. 15. In this plot we show the results with powerlaw spectral model fluctuations using the index of $-13/3$ instead of $-11/3$. The results show little evidence of a signal above the standard deviation of the smooth model results, despite the features seen in Fig. 5. The results appear consistent with below 8 per cent emissivity fluctuations however. The spectrum is below the upper bounds of the 4 and 8 per cent models.

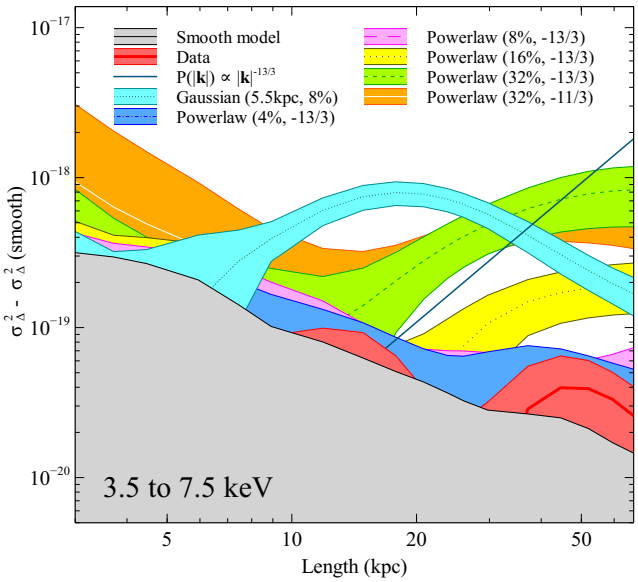


**Figure 15.** Δ-variance spectra for the 3.5 to 7.5 keV band in the 1 to 6.7 arcmin radial region, of the data and model clusters after subtracting the ELFIT model.

### 4.6 Spectra for different cluster models

We can compare how the choice of smooth model for the cluster emission affects the Δ-variance spectrum. We can also examine whether the spectra are different between spatial regions or as a function of radius. In Fig. 16 we show the spectra for the data and simulated data with fluctuations after subtraction of the single $\beta$ model, a two-component $\beta$ model and ELFIT models with 10 and 20 ellipses (shown in Fig. 9 and Fig. 10). Before computing the spectra we again also fit the simulated model images with the model before subtraction of that model to make a fair comparison between the data and model. The results for different smooth models are shown by the rows in Fig. 16. We do the analysis for the standard 1 to 6.7 arcmin radius region (21 to 141 kpc) in the first column, the central 21 to 74 kpc (1 to 3.5 arcmin) in the central column and the outer 74 to 141 kpc (3.5 to 6.7 arcmin) region in the final column.

The choice of smooth model makes a large difference to the resulting power spectra normalisation and shape. Using the $\beta$ model fit, the data have a Δ-variance spectrum similar to the model with the $-11/3$ power spectrum fluctuations, but the normalisation is around 32 per cent in the central region and 16 per cent in the outer region. With the double-$\beta$ model the normalisations are just above 16 and 8 per cent, respectively. With the 10 ELFIT model the cluster shows a Δ-variance spectrum which is even lower still. The 20 ELFIT model produces normalisations which are around 8 per cent (see Section 4.5), on long scales in both the inner and outer regions. On shorter scales there is a peak of signal on scales of around 15 kpc in the outer region.

We can do a similar analysis in the 3.5 to 7.5 keV band (Fig. 17). We use the same type of modelling as for the 0.6 to 5 keV band, except that the data are too poor to fit using the 20 ellipse model. Subtracting a $\beta$ model fit, the data show similar spectra to those of the $-13/3$ powerlaw fluctuations with normalisations close to the wider energy band results, except in the outer region where the normalisation is much lower. The double-$\beta$ model results show power spectra which are only significant on large scales, with values between the 8 and 16 per cent results. Using the ELFIT ellipse fit, there is perhaps a peak in signal around 15 kpc in the outer part of the cluster, but no evidence for the peak in the inner part. There is little evidence for any significant additional fluctuations in any part of the galaxy cluster in this band using the ellipse model, despite being seen in Fig. 5.

## 5 DISCUSSION

The surface brightness image of the galaxy cluster appears remarkably smooth in images (Fig. 1). When examining the full band image, unsharp masking reveals the bright core and an edge to the north-west (Fig. 2). The X-ray emission is extended in the east-west direction relative to the north-south axis and the central X-ray peak is offset west from the larger scale emission (Neumann & Böhringer 1995 and Fig. 9).

When subtracting the smooth ELFIT model fit from the 0.6 to 5 keV data (Fig. 5 top-left panel) there are linear residuals which are not present in simulated realisations of the smooth model (bottom-left panel). The magnitude of the residuals is around 4 per cent of the surface brightness. The strongest features are linear depressions towards the south-west and south-east radiating from the centre. They are also confirmed in *XMM-Newton* EPIC-MOS images (Fig. 6). These residuals are also present in the harder pressure-sensitive 3.5 to 7.5 keV band (Fig. 5 top-right panel).

We show the distribution of surface brightness relative to the ELFIT smooth model in Fig. 7 and Fig. 8. The data show a wider distribution of pixel value than the ELFIT realisations in all four of the elliptical regions shown, examined on scales of 4 and 8 pixels (2.8 and 5.6 kpc, respectively). The data have a narrower distribution than the ELFIT realisations with added projected Gaussian fluctuations with a standard deviation of 4 per cent. The data histograms are not completely consistent with a Gaussian shape, however, and are typically weighted towards small negative deviations and counterbalancing large positive deviations.

The measured deviations are dependent on the surface brightness model subtracted from the cluster image. We examined four different models in Fig. 9 and Fig. 10 for the 0.6 to 5 keV band. The single and two component elliptical $\beta$ models are unable to subtract the smooth cluster emission. The models cannot properly account for the offset of the core, twisting isophotes and edges seen in the residuals in Fig. 10. The residuals, however, do not look like classical hydrodynamical turbulence (e.g. Fig. 11). The residuals to the $\beta$ model fits resemble cold fronts, which are contact discontinuities, seen in data and cluster simulations (e.g. Ascasibar & Markevitch 2006). These features could be due to residual sloshing of gas in the potential well. The ELFIT model with 10 ellipses is also unable to properly model the sharp edge immediately east of the cluster core and further out to the west.

The high level of fluctuations seen in the Δ-variance spectra of the 0.6 to 5 keV band in the top three rows of Fig. 16 appears mostly due to the large scale edges and offsets seen in Fig. 10. When these features are subtracted by the 20 ELFIT model the Δ-variance spectra are significantly reduced on large scales (see Fig. 13 or bottom row of Fig. 16). If the subtraction of the ELFIT model removed the turbulence-like powerlaw noise, we would be unable to differentiate the models with varying amounts of fluctuations in Fig. 13. This is because we apply the same model-fitting analysis to the simulated data as the real data. The ELFIT modelling removes contact-discontinuities which would be invisible in a pressure map of the cluster.

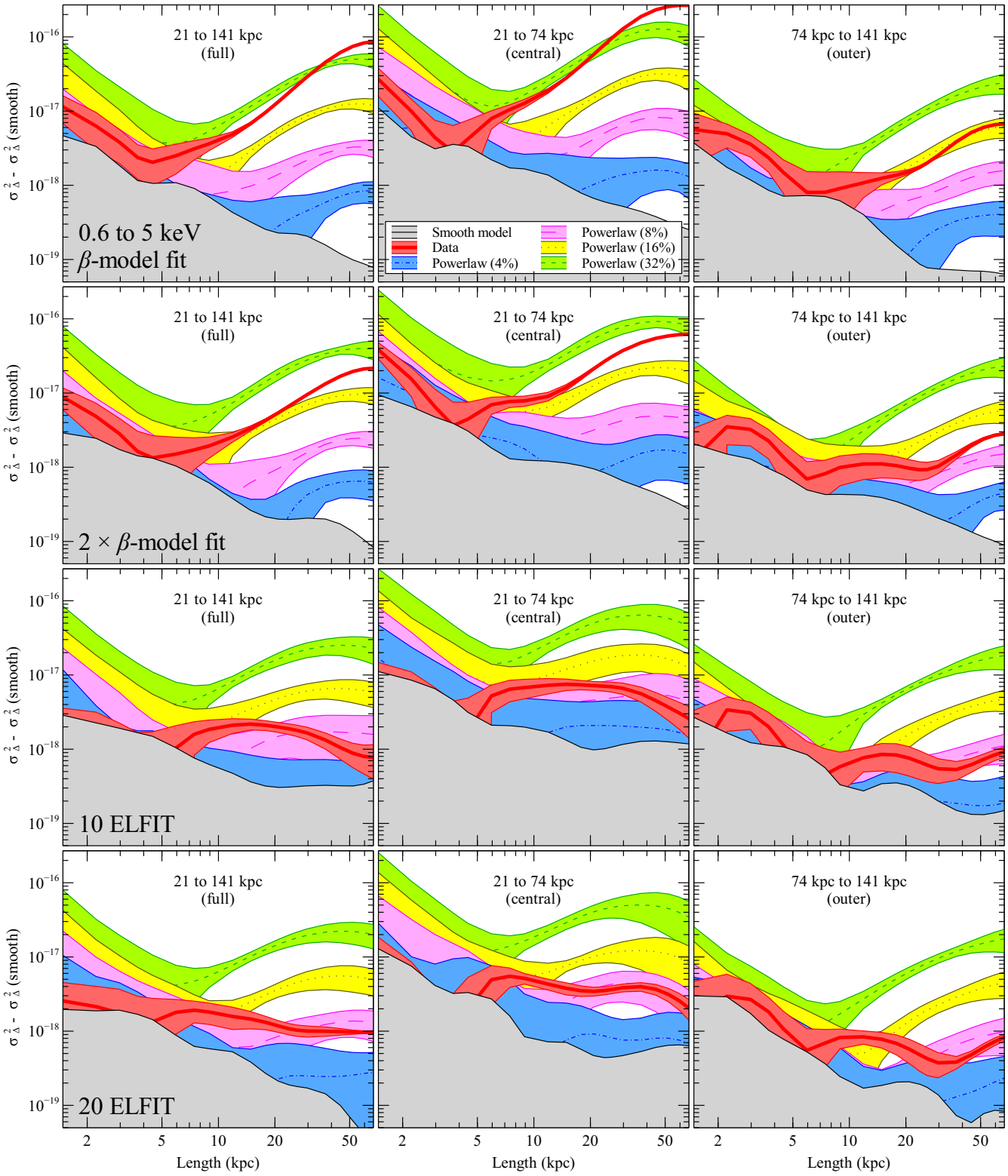


**Figure 16.** Δ-variance spectra for the 0.6 to 5 keV band in the 1 to 6.7 arcmin radial region (left), 1 to 3.5 arcmin (centre) and 3.5 to 6.7 arcmin (right) regions, after subtraction of the smooth model spectra. The rows show the result of subtracting different models for the cluster surface brightness. The top row is for a $\beta$ model fit to the surface brightness, outside 1 arcmin. The second row is for a 2 component $\beta$ model, fitted to the whole *Chandra* region. The third and fourth rows show the results using ELFIT models with 10 and 20 ellipses, respectively. Within each panel we show the spectra of the data (red), a model without any fluctuations (grey), models with powerlaw power spectra with an index of $-11/3$ (dark blue, pink, yellow and green, with increasing normalisation).

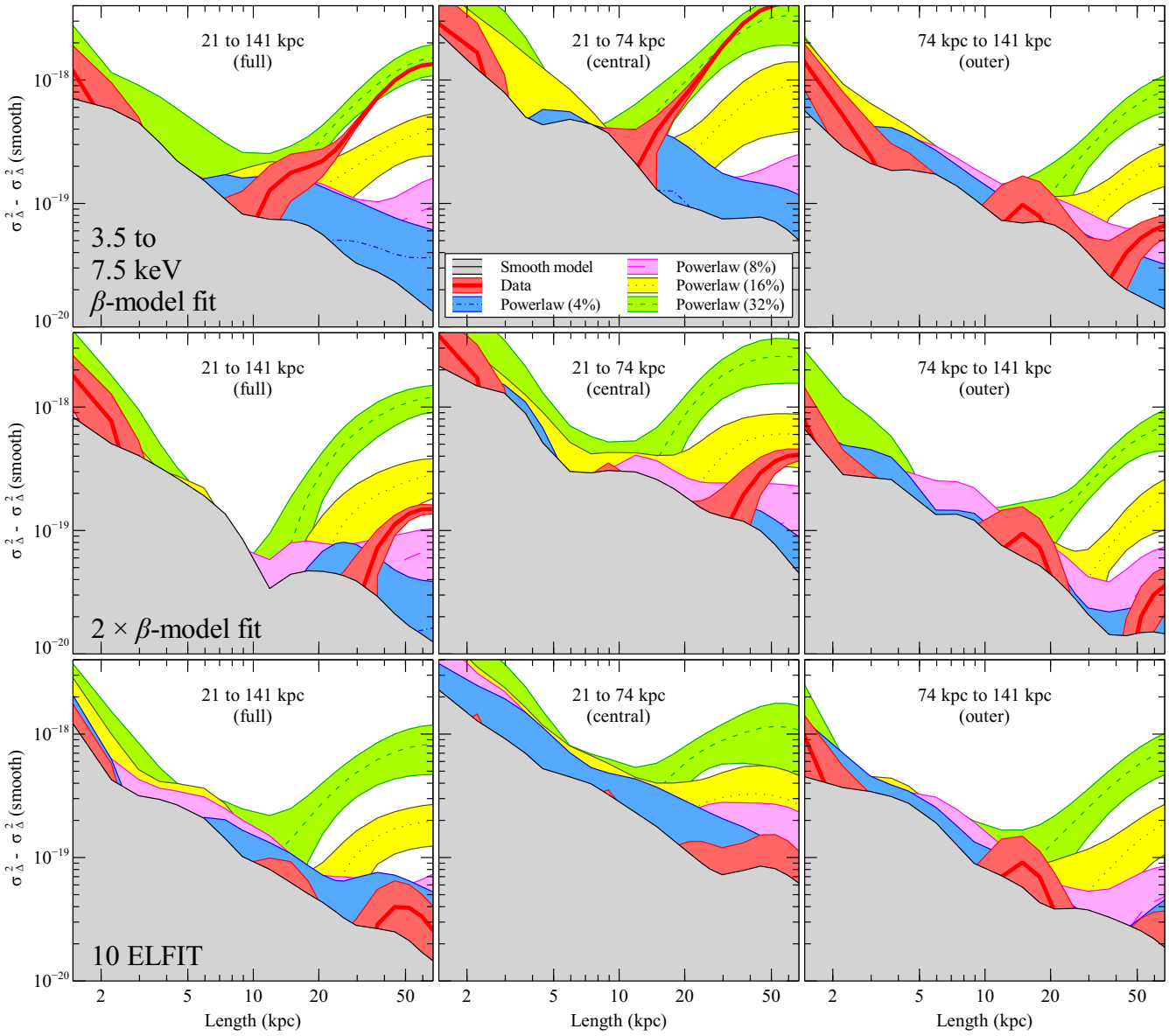


**Figure 17.** Δ-variance spectra in the 3.5 to 7.5 keV band, similarly to Fig. 16. We do not include the 20 ELFIT model as there are not enough data. The powerlaw power spectrum models use a spectral index of $-13/3$, rather than $-11/3$.

We therefore detect fluctuations in the 0.6 to 5 keV data, but the magnitude of these features is lower compared to many of our models. The model with a spectrum nearest to the data on longer scales has 3D emissivity deviations with an 8 per cent standard deviation and a power spectrum index of -11/3. The shape of the power spectrum from the data appears to be flatter, however, with an index of between $-5/3$ and $-6/3$ at long scales. The amount of power on small scales is smaller than the lowest powerlaw which has 4 per cent fluctuations. There is a peak in the Δ-variance spectrum on scales of around 15 kpc. The shape of the data spectrum is similar to the Gaussian projected fluctuation model, but is less peaked. We note that when comparing the spectrum of the data with the model spectra, that the model spectra are normalised on length scales of zero to 150 kpc.

If we compare the spectra of the inner part of the cluster to the outer part (centre and right panels of the bottom row of Fig. 16), then the central region has a flatter spectrum than the outer region. Ignoring the high small scale power, the outer region roughly follows the 8 per cent powerlaw power spectrum model. The central region contributes to the peak in the total Δ-variance spectrum, peaking on scales of 15 to a few 10s of kpc.

If we assume that the level of emissivity fluctuations in the 0.6 to 5 keV band has a standard deviation of 8 per cent then the corresponding standard deviation for density fluctuations is 4 per cent. This value is surprisingly close to the 5 per cent value seen on small scales in in the Coma cluster (Churazov et al. 2011), despite AWM 7 appearing to be a more relaxed object on large scales.

We can test whether the radial depressions to the south of the core of the cluster are the main contribution to the shape of the Δ-variance spectrum. We computed the spectra for the northern and southern sectors of the cluster independently in the 0.6 to 5 keV band, between radii of 1 and 6.7 arcmin, after subtraction of the ELFIT model (Fig. 18). These spectra have the noise removed by the subtraction of the spectrum of a model-subtracted realisation

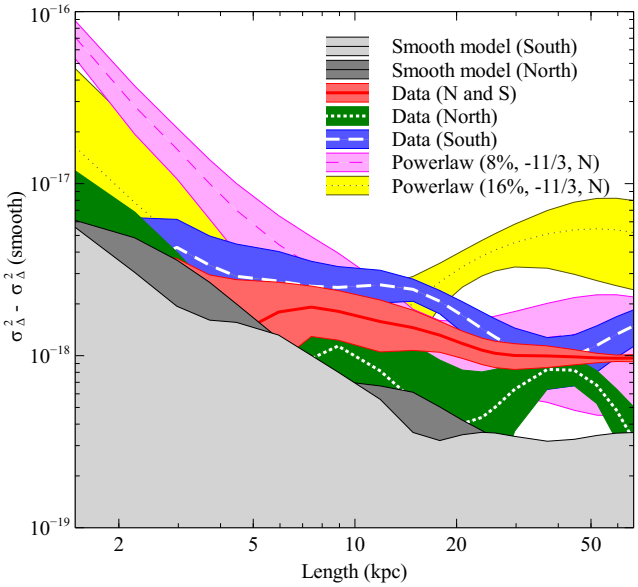


**Figure 18.** Δ-variance spectra for the northern and southern halves of the cluster, examining the radii between 1 and 6.7 arcmin. An ELFIT model was subtracted before the spectra were calculated and the mean smooth model spectrum was subtracted from each plotted spectrum, similarly to Fig. 13. The green (thick dotted) and purple (thick dashed) regions show the spectrum of the data in the north and south, respectively. The red (thick solid) spectrum is for both halves. The two grey shaded regions at the bottom of the plot are the standard deviations of realisations of the ELFIT model in the northern and southern halves.The yellow (light dotted) region shows a spectrum for a model with powerlaw power spectra with 16 per cent fluctuations and an index of -11/3 and the pink (light dashed) region is the same with an 8 per cent normalisation.

of the ELFIT model, as in Fig. 13. Also shown in the plot is the spectrum of the both halves of the cluster, and the spectrum of a model with a powerlaw power spectrum fluctuations normalised to have 16 per cent standard deviation. The southern region, which contains the radial depressions, shows more power than in the north on virtually all length scales.

The normalisation of the north spectrum on long scales is roughly consistent with the powerlaw power spectrum with a normalisation of around 4 per cent. The implied density variations are therefore around 2 per cent in the north.

There will be some contribution to surface brightness fluctuations due to small scale metallicity fluctuations. Such metal features are found in several other clusters, e.g. Perseus (Sanders et al. 2004; Sanders & Fabian 2007) and Abell 2204 (Sanders et al. 2009). The importance of this effect at the predominant $\sim 3.5$ keV temperature of this cluster is small. 20 per cent enhancements in metallicity from $0.3\,Z_\odot$ only increase the 0.6 to 5 keV surface brightness by $\sim 2.5$ per cent.

Examining the pressure-squared-sensitive 3.5 to 7.5 keV band, the Δ-variance spectra (Fig. 15 and Fig. 17) are harder to differentiate from the smooth ELFIT model spectra. On scales of greater than 5 kpc they are roughly consistent with powerlaw model emissivity variations normalised to 4 or 8 per cent, although there appears to be some signal on scales of 15 kpc in the outer region and on longer scales in the central region. If the pressure fluctuations are half the emissivity variations, the standard deviation of pressure fluctuations is less than 4 per cent.

We therefore find that there are significant fluctuations in the surface brightness of AWM 7, but they are of a low level. The standard deviation of thermal pressure fluctuations is less than 4 per cent. These values are smaller than the lower limit found for the Coma cluster of 10 per cent (Schuecker et al. 2004). AWM 7, however, is a much more relaxed cluster than the dynamically disturbed Coma cluster. AWM 7 is not a prototypical relaxed, cool-core cluster, however, as it has a small, cool core and its isophotes are twisted. We will show in a later paper that the temperature profile is largely isothermal over the 25 to 250 kpc radius region.

Churazov et al. (2010) compared X-ray observations of hot gas and stellar circular speed for several elliptical galaxies, finding that the non-thermal pressure, on average, is 20 to 30 per cent of the thermal gas pressure. This value is much larger than the level of pressure deviation we could attribute to turbulence. If these elliptical galaxies had similar levels of turbulence to AWM 7 then it would require most of this pressure to be due to other sources such as cosmic rays or magnetic fields.

Some caution must be exercised when interpreting our results, however. The conversion from observed surface brightness to density or pressure depends on the assumption that the dominant pressure contribution is thermal in origin. Real galaxy clusters are known to contain relativistic particles and magnetic fields. If these components of the cluster affect the thermal gas on the scales examined, the interpretation becomes much less straightforward. In addition, non-equilibrium thermal processes may become important under some conditions. If non-thermal effects are important, we would not be able to simply compare the observed power spectral index against the Kolmogorov value. It would be very valuable to create mock observations from simulations incorporating relativistic particles and magnetic fields, to help interpret our results.

The simulations of Vazza et al. (2011) find the ratio of turbulent to thermal energy in relaxed clusters ranges from 2 to 8 per cent. If we characterise the detected fluctuations in AWM 7 as turbulence, our results are consistent with this range of values. Vazza et al. (2011), however, do not yet probe scales below 25 kpc $h^{-1}$, so we cannot make a direct comparison using the same analysis method as applied to the data. In addition, the effect of the activity of the central nucleus is not included in these simulations and may be important for the shape of spectrum observed.

Some of the signal in the Δ-variance spectrum from the central regions may be related to the activity of the central nucleus. Feedback by the supermassive black holes in galaxy clusters can create ripples in surface brightness interpreted as sound waves, seen in the Perseus (Fabian et al. 2003a; Sanders & Fabian 2007), Centaurus (Sanders & Fabian 2008) and Abell 2052 (Blanton et al. 2009) galaxy clusters. Sound waves should give rise to characteristic length scale in the Δ-variance spectrum at some level, although at their expected magnitude they are very hard to detect in all but the nearest and brightest clusters with current telescopes (Graham et al. 2008).

In this paper we have not taken advantage of the spectral information available in the data. We will investigate the distribution of pressure fluctuations using measured temperature and density in a future paper. We will also examine the cool X-ray core itself.

## 6 CONCLUSIONS

We examine deep *Chandra* and *XMM-Newton* images of the bright AWM 7 galaxy cluster. After representing the large scale surface brightness distribution with a model made by interpolating ellipses fitted to surface brightness contours, we find residual features which are approximately radial, have a projected magnitude

of 4 per cent in the 0.6 to 5 keV band and are strongest in the south of the cluster. Examining the 3.5 to 7.5 keV band, which is more sensitive to pressure variations, we also find evidence for such features at a similar magnitude.

A histogram of the surface brightness distribution after subtraction of a smooth model also shows a wider distribution than expected from the Poisson statistics.

If, instead of the ELFIT model for the surface brightness, we fit a $\beta$ or double-$\beta$ model to the cluster, the residuals are considerably larger because of the offset peak in X-ray emission in this cluster and a number of edges in surface brightness.

We use $\Delta$-variance spectra to characterise the scales on which the fluctuations occur. The magnitude of the fluctuations is roughly consistent with a model with powerlaw power spectra with an index and a standard deviation of 8 per cent pressure fluctuations in 3D emissivity the 0.6 to 5 keV band. The spectrum appears flatter than expected, however. The implied density fluctuations have a standard deviation of around 4 per cent. In the pressure-squared-sensitive 3.5 to 7.5 keV band, the 3D pressure fluctuations appear to be 4 per cent or less.

We find that there is a large difference between the signal in the $\Delta$-variance spectra between the north and south of the cluster. On the longest scales there is roughly a factor of two less $\Delta$-variance signal in the north relative to the south.

## ACKNOWLEDGEMENTS

The authors thank E. Churazov for giving a talk making them aware of the $\Delta$-variance method. ACF acknowledges the support of the Royal Society.

## REFERENCES

Armstrong J. W., Rickett B. J., Spangler S. R., 1995, ApJ, 443, 209
Ascasibar Y., Markevitch M., 2006, ApJ, 650, 102
Beers T. C., Kriessler J. R., Bird C. M., Huchra J. P., 1995, AJ, 109, 874
Blanton E. L., Randall S. W., Douglass E. M., Sarazin C. L., Clarke T. E., McNamara B. R., 2009, ApJ, 697, L95
Brüggen M., Hoeft M., Ruszkowski M., 2005, ApJ, 628, 153
Cavagnolo K. W., Donahue M., Voit G. M., Sun M., 2009, ApJS, 182, 12
Churazov E., Forman W., Jones C., Sunyaev R., Böhringer H., 2004, MNRAS, 347, 29
Churazov E., Forman W., Vikhlinin A., Tremaine S., Gerhard O., Jones C., 2008, MNRAS, 388, 1062
Churazov E. et al., 2010, MNRAS, 404, 1165
Churazov E. et al., 2011, submitted, preprint, arXiv:1110.5875
Dutta P., Begum A., Bharadwaj S., Chengalur J. N., 2009, MNRAS, 398, 887
Edge A. C., Stewart G. C., Fabian A. C., 1992, MNRAS, 258, 177
Fabian A. C., Sanders J. S., Allen S. W., Crawford C. S., Iwasawa K., Johnstone R. M., Schmidt R. W., Taylor G. B., 2003a, MNRAS, 344, L43
Fabian A. C., Sanders J. S., Crawford C. S., Conselice C. J., Gallagher J. S., Wyse R. F. G., 2003b, MNRAS, 344, L48
Forman W. et al., 2007, ApJ, 665, 1057
Furusho T., Yamasaki N. Y., Ohashi T., 2003, ApJ, 596, 181
Graham J., Fabian A. C., Sanders J. S., 2008, MNRAS, 391, 1749
Hatch N. A., Crawford C. S., Johnstone R. M., Fabian A. C., 2006, MNRAS, 367, 433
Heinz S., Brüggen M., Morsony B., 2010, ApJ, 708, 462
Kim J., Ryu D., 2005, ApJ, 630, L45
Koranyi D. M., Geller M. J., 2000, AJ, 119, 44
Koranyi D. M., Geller M. J., 2002, AJ, 123, 100
Kowal G., Lazarian A., Beresnyak A., 2007, ApJ, 658, 423
Kuntz K. D., Snowden S. L., 2008, A&A, 478, 575
Kunz M. W., Schekochihin A. A., Cowley S. C., Binney J. J., Sanders J. S., 2011, MNRAS, 410, 2446
Lau E. T., Kravtsov A. V., Nagai D., 2009, ApJ, 705, 1129
Lesieur M., 2008, Turbulence in fluids. Springer, Dordrecht
McNamara B. R., Nulsen P. E. J., 2007, ARA&A, 45, 117
Neumann D. M., Böhringer H., 1995, A&A, 301, 865
Ossenkopf V., Krips M., Stutzki J., 2008, A&A, 485, 719
Peres C. B., Fabian A. C., Edge A. C., Allen S. W., Johnstone R. M., White D. A., 1998, MNRAS, 298, 416
Sanders J. S., 2006, MNRAS, 371, 829
Sanders J. S., Fabian A. C., 2007, MNRAS, 381, 1381
Sanders J. S., Fabian A. C., 2008, MNRAS, 390, L93
Sanders J. S., Fabian A. C., Allen S. W., Schmidt R. W., 2004, MNRAS, 349, 952
Sanders J. S., Fabian A. C., Smith R. K., 2011, MNRAS, 410, 1797
Sanders J. S., Fabian A. C., Smith R. K., Peterson J. R., 2010, MNRAS, 402, L11
Sanders J. S., Fabian A. C., Taylor G. B., 2009, MNRAS, 393, 71
Sato K., Matsushita K., Ishisaki Y., Yamasaki N. Y., Ishida M., Sasaki S., Ohashi T., 2008, PASJ, 60, 333
Schuecker P., Finoguenov A., Miniati F., Böhringer H., Briel U. G., 2004, A&A, 426, 387
Smith R. K., Brickhouse N. S., Liedahl D. A., Raymond J. C., 2001, ApJ, 556, L91
Stanimirovic S., Staveley-Smith L., Dickey J. M., Sault R. J., Snowden S. L., 1999, MNRAS, 302, 417
Stutzki J., Bensch F., Heithausen A., Ossenkopf V., Zielinsky M., 1998, A&A, 336, 697
Vazza F., Brunetti G., Gheller C., Brunino R., Brüggen M., 2011, A&A, 529, A17
Vazza F., Brunetti G., Kritsuk A., Wagner R., Gheller C., Norman M., 2009, A&A, 504, 33
Werner N., Zhuravleva I., Churazov E., Simionescu A., Allen S. W., Forman W., Jones C., Kaastra J. S., 2009, MNRAS, 398, 23